Microwave Subsurface Imaging Method by Incorporating Radar and Tomographic Approaches

Shuto Takahashi, *Member, IEEE*, Katsuyoshi Suzuki, Takahiro Hanabusa, and Shouhei Kidera, *Senior Member, IEEE*

***Abstract*— Due to its high resolution and deep penetration depth, microwave ultrawideband radar is a promising tool for the non-destructive testing (NDT) of transportation infrastructure. Microwave radiation can also be used to reconstruct the dielectric properties of objects and therefore can be used to detect an air cavity or metallic rust in concrete. We used contrast source inversion (CSI) as one of the most promising inverse scattering schemes. To resolve the observation domain limitations of NDT, radar imaging method, also known as range points migration (RPM) method, was first incorporated into the inverse scattering algorithm based on CSI as a region of interest (ROI) estimator, which substantially improves the accuracy of complex permittivity reconstruction. In addition, the ROI optimizing scheme based on the CSI cost function is used to enhance ROI accuracy. The effectiveness of the proposed methods is validated via finite-difference time-domain (FDTD)-based numerical simulation, which assumes typical NDT model.**

***Index Terms*— Contrast source inversion method (CSI), inverse scattering problem, microwave non-destructive testing (NDT), radar imaging, range points migration (RPM).**

I. Introduction

THE aging of transportation infrastructure such as tunnels and highways predisposes them to a higher risk of collapse or severe damage by an earthquake, which frequently occurs in Japan. A significant percentage of Japanese transportation infrastructure was built during the high economic growth period. In the next 15 years, the ratio of facilities 50 years or older is expected to rapidly rise. Thus, a speedy and accurate nondestructive inspection technique is urgently needed. The conditions inside concrete structures such as bridges and tunnels can be inspected using traditional tools such as ultrasonic testing and hammer tests. Sensors used for ultrasonic testing are inexpensive and provide high resolution. However, they suffer from severe attenuation while propagating in the air. The hammer test is another traditional inspection tool in which a hammer is used to tap a concrete structure, and the presence of cavities inside the concrete is determined based on the differences in the resulting sound. This method also requires proximity to the test site. Thus, both methods require contact measurement, and a large-scale inspection costs a substantial amount of time and expenses. In contrast, microwave nondestructive testing (NDT) enables noncontact and in situ assessment of microcracking, porosity, chloride ingress, or corroded reinforced rod in aging infrastructure [1]. Microwave-based NDT techniques have many advantages over ultrasonic and hammer tests because they provide deep penetration depth and higher range resolution while preventing severe propagation losses in the air [2].

Various methods have been developed for microwave imaging for subsurface imaging scenarios. These methods can be categorized into two types. The first type is the radar approach based on coherent or incoherent integration of reflection signals. This type provides the position and shape of buried objects such as air, plastic, or metallic materials with relatively high contrast from those of concrete. Most radar approaches are based on the coherent integration process, such as synthetic aperture radar (SAR) [3], [4], multidimensional beam-forming, and the Kirchhoff migration method [5], [6]. In addition, a more accurate and higher spatial resolution radar imaging approach called the range points migration (RPM) method has been developed [7]. The RPM method converts the measured range-associated sensor locations (called range points) to corresponding scattering centers on the object's boundary. Its effectiveness has been demonstrated in many studies, including NDT [8], [9], [10]. However, these methods do not extract quantitative values of the dielectric properties of objects, such as complex permittivity. Some studies [11] demonstrated that different rust types (e.g., black rust, salt rust, and red rust) exhibit different complex permittivities; thus, quantitative material characterization becomes important for NDT [12], [13].

The second type of microwave imaging method is inverse scattering analysis based on the solution of the domain integral equation. This type offers a quantitative estimate of the complex permittivity map. However, the above inverse problem has a nonlinear and ill-posed nature. Thus, several approaches, such as diffraction tomography, born iterative method (BIM), distorted BIM (DBIM) [14], [15], and contrast source inversion (CSI) [16], [17], [18], are used to solve the above type of inverse problem, where various types of

Manuscript received 13 March 2022; accepted 23 June 2022. Date of publication 10 October 2022; date of current version 17 November 2022. This work was supported by the Commissioned Research of the "National Institute for Land and Infrastructure Management," Under Technology Research and Development System of "The Committee on Advanced Road Technology" Established by the Ministry of Land, Infrastructure, Transport and Tourism (MLIT), Japan. *(Corresponding author: Shouhei Kidera.)*

The authors are with the Graduate School of Informatics and Engineering, The University of Electro-Communications, Chofu 182-8585, Japan (e-mail: kidera@uec.ac.jp).

Color versions of one or more figures in this article are available at https://doi.org/10.1109/TAP.2022.3188358.

Digital Object Identifier 10.1109/TAP.2022.3188358

This work is licensed under a Creative Commons Attribution-NonCommercial-NoDerivatives 4.0 License.
For more information, see https://creativecommons.org/licenses/by-nc-nd/4.0/

extensions have been introduced such as multiplicative regularization (MR)-CSI, cross-correlated (CR)-CSI [19], contrast source extended born inversion (CSEB) [20], or finite-element method (FEM)-CSI [21]. Focusing on the CSI scheme, significant performances have been reported in biomedical applications [22], [23], [24], such as ground-penetrating radar-based subsurface imaging [25], [26], [27], [28], [29], [30], and through-the-wall imaging applications [31], [32]. However, for a typical NDT scenario, the tomographic measurement data are hardly available, and the traditional inverse scattering algorithms might face a fatal problem due to the lack of measured data. In addition, a large number of unknowns should be processed for a large-scale search area, which incurs high computational costs and introduces inaccuracies. One of the promising approaches is based on sparse regularization schemes such as compressed sensing, and various algorithms, including the NDT model [33], [34], have been introduced, where the linear or non-linear data conversion is introduced to represent the sparse model. In addition, the hybrid approach with a deep learning scheme to the non-linear inverse scattering problem has been recently developed [35], [36], where an intrinsic non-linearity due to a high-contrast object could be solved by a complex-valued convolution neural network.

Given this background and the limitations of existing approaches, this article proposes a bi-directional updating algorithm between radar and tomographic images, developing on the basic idea proposed in [37] and [38], but they are based on the DBIM. The CSI method was used as its effectiveness has been demonstrated in various applications. In the proposed method, at first, the region of interest (ROI) in the CSI formulation was limited to the vicinity area around the object, which is estimated by the radar-based RPM method [10]. The RPM offers an accurate estimate of the ROI and reduces the number of unknowns processed in the CSI, thereby enhancing the reconstruction accuracy and convergence speed, even in significantly ill-posed situations. This is an advantage of the proposed method, which involves one direction of processing from the radar to tomography, to enhance the CSI's reconstruction performance. On the contrary, an RPM image forms a point-cloud image, and the proposed method converts the RPM image to a distributed image via a Gaussian mixture model (GMM), using a CSI cost function to determine an appropriate ROI for the CSI method. This is the reversal direction, namely, from tomography to radar, which enhances the ROI accuracy. While there have been several studies on ROI limitation or multiscale reconstruction in the inverse scattering scheme [23], [39], [40], [41], these approaches have not considered simultaneously optimizing between radar and inverse scattering analysis, However, this study introduces a novel radar imaging method as RPM in which its limiting ROI is optimized using the CSI cost function. To summarize, the novelty of this study relies on the fact that the RPM-based ROI limitation is first applied to the CSI inversion scheme to enhance the reconstruction accuracy in both the ROI and dielectric property of buried objects. The finite-difference time-domain (FDTD)-based numerical tests, which assumed a typical NDT situation in which an air cavity and some types of metallic rusts were buried in concrete, demonstrated that the ROI limited scheme, rather than the original CSI, would be effective for more accurate dielectric profile reconstruction, and the ROI optimizing scheme would significantly improve the shape and location of objects.

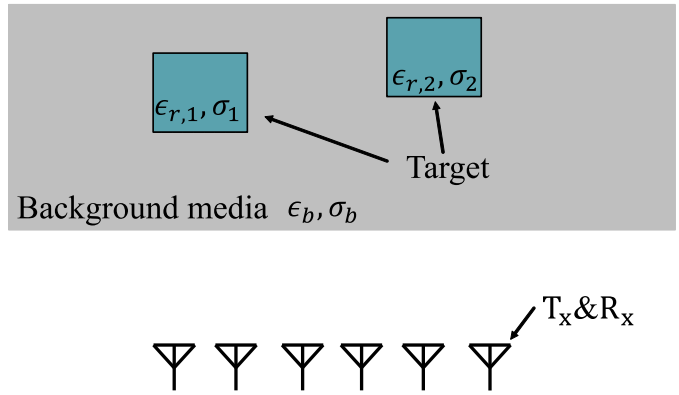

Fig. 1. Observation model.

II. Method

A. Observation Model

Fig. 1 shows a general observation model being applicable to the method presented in this article, where a homogeneous, low-loss, and nondispersive dielectric background medium was assumed. A number of transmitting and receiving antennas were arranged in front of the background media. $E^{\mathrm{T}}(\omega; \boldsymbol{r}_{\mathrm{t}}, \boldsymbol{r}_{\mathrm{r}})$ expresses a total electric field recorded at a receiver located with position $\boldsymbol{r}_{\mathrm{r}}$, which is scattered by media including objects from the source point with position $\boldsymbol{r}_{\mathrm{t}}$, at a specific angular frequency ω. In this 2-D model, we assume the transverse magnetic mode wave in the exciting source, and thus a single polarization component along the z-axis is considered. Then, its scattered electric field $E^{\mathrm{S}}(\omega; \boldsymbol{r}_t, \boldsymbol{r}_r)$ is denoted as follows:

$$E^{\mathrm{S}}(\omega; \boldsymbol{r}_t, \boldsymbol{r}_r) \equiv E^{\mathrm{T}}(\omega; \boldsymbol{r}_t, \boldsymbol{r}_r) - E^{\mathrm{I}}(\omega; \boldsymbol{r}_t, \boldsymbol{r}_r) \tag{1}$$

$E^{\mathrm{I}}(\omega; \boldsymbol{r}_t, \boldsymbol{r}_r)$ denotes the incident electric fields measured in the case without objects. Ω_{S} and Ω_{D} denote regions including the observation array and object, respectively. Note that a complex permittivity of background media is provided. Here, the inverse transform of $E^{\mathrm{S}}(\omega; \boldsymbol{r}_{\mathrm{t}}, \boldsymbol{r}_{\mathrm{r}})$ is defined as $e(t; \boldsymbol{r}_{\mathrm{t}}, \boldsymbol{r}_{\mathrm{r}})$, and its filter output (e.g., matched filter) is defined as $e(R; \boldsymbol{r}_{\mathrm{t}}, \boldsymbol{r}_{\mathrm{r}})$, where $R = \mathrm{c}t/2$, t is time and c is the speed of light in the air. The range points extracted from the local maxima of $e(t; \boldsymbol{r}_{\mathrm{t}}, \boldsymbol{r}_{\mathrm{r}})$ to R are divided into two groups. One is defined as $\boldsymbol{q}_{1,i} \equiv (\boldsymbol{r}_{\mathrm{t},i}, \boldsymbol{r}_{\mathrm{r},i}, R_{1,i})$, where each member has a maximum $e(t; \boldsymbol{r}_{\mathrm{t}}, \boldsymbol{r}_{\mathrm{r}})$ to R. The remaining range points are classified as $\boldsymbol{q}_{2,i} \equiv (\boldsymbol{r}_{\mathrm{t},i}, \boldsymbol{r}_{\mathrm{r},i}, R_{2,i})$. Note that R_1 defined in $\boldsymbol{q}_1$ is the distance from the observation point to a surface of concrete media propagating in air, whereas $R_2 - R_1$ with $\boldsymbol{q}_2$ is the distance from a concrete surface to an object propagating into concrete media. To deal with these variables uniformly, they are first defined using the propagation speed in the air.

B. Contrast Source Inversion (CSI)

In this study, we focused on CSI as one of the most promising inverse scattering algorithms for NDT via dielectric

profile reconstruction because it enables us to reconstruct a dielectric profile without requiring an iterative calculation by a forward solver. This section summarizes the theory and methodology of the original CSI. Here, to simplify the notation in each variable, $E^{\mathrm{T}}(\omega; \boldsymbol{r}_t, \boldsymbol{r}_r)$, $E^{\mathrm{I}}(\omega; \boldsymbol{r}_t, \boldsymbol{r}_r)$, and $E^{\mathrm{S}}(\omega; \boldsymbol{r}_t, \boldsymbol{r}_r)$ are redefined as $E^{\mathrm{T}}_{j,k}(\boldsymbol{r}_r)$, $E^{\mathrm{I}}_{j,k}(\boldsymbol{r}_r)$ and $E^{\mathrm{S}}_{j,k}(\boldsymbol{r}_r)$, respectively, where k and j denote the index number of the sources and frequency, respectively. The scattered field, $E^{\mathrm{S}}_{j,k}(\boldsymbol{r}_r)$, is defined using the following domain integral as follows:

$$\begin{aligned} E^{\mathrm{S}}_{j,k}(\boldsymbol{r}_r) &\equiv E^{\mathrm{T}}_{j,k}(\boldsymbol{r}_r) - E^{\mathrm{I}}_{j,k}(\boldsymbol{r}_r) \\ &= k_{\mathrm{b}}^2 \int_{\Omega_{\mathrm{D}}} G^{\mathrm{b}}_j(\boldsymbol{r}_r, \boldsymbol{r}') E^{\mathrm{T}}_{j,k}(\boldsymbol{r}') O_j(\boldsymbol{r}') d\boldsymbol{r}', \quad (\boldsymbol{r}_r \in \Omega_{\mathrm{S}}) \end{aligned} \tag{2}$$

where k_{b} and $G^{\mathrm{b}}_j(\boldsymbol{r}_r, \boldsymbol{r}')$ represent the wavenumber and Green's function of the background media, respectively. Ω_{S} and Ω_{D} are defined as the observation domain and the object domain, also known as the ROI, respectively. $E^{\mathrm{T}}_{j,k}(\boldsymbol{r})$ denotes the total field, whereas $O_j(\boldsymbol{r}) = (\epsilon_j(\boldsymbol{r}) - \epsilon_{\mathrm{b},j}(\boldsymbol{r}))/\epsilon_{\mathrm{b},j}(\boldsymbol{r})$ represents the contrast function, where $\epsilon(\boldsymbol{r})$ and $\epsilon_{\mathrm{b}}(\boldsymbol{r})$ denote the complex permittivities of the object and background media at location $\boldsymbol{r}$, respectively.

Here we introduce a variable defined as $w_{j,k}(\boldsymbol{r}) \equiv O_j(\boldsymbol{r}) E^{\mathrm{T}}_{j,k}(\boldsymbol{r})$, known as "contrast source." Using this variable, (2) can be rewritten as follows:

$$\begin{aligned} E^{\mathrm{S}}_{j,k}(\boldsymbol{r}_r) &\equiv E^{\mathrm{T}}_{j,k}(\boldsymbol{r}_r) - E^{\mathrm{I}}_{j,k}(\boldsymbol{r}_r) \\ &= k_{\mathrm{b}}^2 \int_{\Omega_{\mathrm{D}}} G^{\mathrm{b}}_j(\boldsymbol{r}_r, \boldsymbol{r}') w_{j,k}(\boldsymbol{r}') d\boldsymbol{r}', \quad (\boldsymbol{r}_r \in \Omega_{\mathrm{S}}). \end{aligned} \tag{3}$$

Equation (3), also called the data equation, expresses the same physical phenomena as (2). Notably, instead of using the forward solver, the following equation holds for the CSI method:

$$E^{\mathrm{T}}_{j,k}(\boldsymbol{r}) = E^{\mathrm{I}}_{j,k}(\boldsymbol{r}) + k_{\mathrm{b}}^2 \int_{\Omega_{\mathrm{D}}} G^{\mathrm{b}}_j(\boldsymbol{r}, \boldsymbol{r}') w_{j,k}(\boldsymbol{r}') d\boldsymbol{r}', \quad (\boldsymbol{r} \in \Omega_{\mathrm{D}}). \tag{4}$$

Equation (4), also called the state equation, is also derived from (2). Note that, this equation is used to obtain the total field in any location within the object domain Ω_{D}, namely, the ROI, and since $E^{\mathrm{T}}_{j,k}(\boldsymbol{r})$ is included on both sides of the equation, it expresses the nonlinearity of the scattering phenomenon, including multiple scattering. The solution to the "state equation" corresponds to the solution obtained by the assumed forward problem. The original CSI introduces the following cost function:

$$F(w_{j,k}(\boldsymbol{r}), O_j(\boldsymbol{r})) \equiv F^S(w_{j,k}(\boldsymbol{r})) + F^D(w_{j,k}(\boldsymbol{r}), O_j(\boldsymbol{r})) \tag{5}$$

where

$$\begin{aligned} &F^S(w_{j,k}(\boldsymbol{r})) \\ &\equiv \frac{1}{J} \sum_j \frac{\sum_k \left\| E^{\mathrm{S}}_{j,k}(\boldsymbol{r}_r) - k_{\mathrm{b}}^2 \int_{\Omega_{\mathrm{D}}} G^{\mathrm{b}}_j(\boldsymbol{r}_r, \boldsymbol{r}') w_{j,k}(\boldsymbol{r}') d\boldsymbol{r}' \right\|^2_{\Omega_{\mathrm{S}}}}{\sum_k \left\| E^{\mathrm{S}}_{j,k}(\boldsymbol{r}_r) \right\|^2_{\Omega_{\mathrm{S}}}} \end{aligned} \tag{6}$$

$$\begin{aligned} &F^D(w_{j,k}(\boldsymbol{r}), O_j(\boldsymbol{r})) \\ &\equiv \frac{1}{J} \sum_j \frac{\sum_k \left\| O_j(\boldsymbol{r}) E^{\mathrm{T}}_{j,k}(\boldsymbol{r}) - w_{j,k}(\boldsymbol{r}) \right\|^2_{\Omega_{\mathrm{D}}}}{\sum_k \left\| O_j(\boldsymbol{r}) E^{\mathrm{I}}_{j,k}(\boldsymbol{r}) \right\|^2_{\Omega_{\mathrm{D}}}} \end{aligned} \tag{7}$$

holds. Equations (7) and (6) denote the normalized residual between the left and right sides of (2) and (4), respectively. Here, $\|*\|_{\Omega_{\mathrm{S}},\Omega_{\mathrm{D}}}$ denotes l_2 norm on Ω_{S} and Ω_{D}. The CSI reconstructs $O_j(\boldsymbol{r})$, by sequentially updating $w_{j,k}(\boldsymbol{r})$, $O_j(\boldsymbol{r})$ and $E^{\mathrm{T}}_{j,k}(\boldsymbol{r})$ to minimize the cost function in (5). A notable feature of the CSI is that it avoids the use of computationally expensive forward solvers (e.g., FDTD), by simultaneously solving the "data" and "state" equations.

C. Bi-Directional Updating Algorithm With CSI and RPM

Generally, while CSI assumes that tomographic observation, namely, omnidirectional scattered data, is available in the NDT model, such omnidirectional data are hardly available, which makes the problem more ill-posed and incurs inaccuracies or sluggish convergence in the reconstruction. However, it is expected that an air cavity, crack, or reinforced pipe with erosion is sparsely distributed in most cases; hence, the ROI restriction for the above objects would only significantly decrease the number of unknowns. Nonetheless, an accurate ROI is required as prior information for the inverse scattering algorithm. As a solution to the above issue, this article introduces a radar-based ROI restriction and updating scheme for the CSI method to obtain a more accurate and computationally efficient solution.

The major approach for radar imaging is based on the coherent integration process, represented by SAR, range migration algorithm (RMA), or Kirchhoff migration, where the azimuth resolution can be enhanced by a coherent process. The process has been demonstrated in various observation models, including subsurface imaging. However, the spatial resolution or accuracy of the method is limited for the shape reconstruction of buried objects because coherent-based algorithms assume that the scattering point is invariant with respect to the observation point, and in the case of continuously shaped boundaries, the dominant scattering center moves along its boundary, thereby making the above assumption invalid and incurring inaccuracy in shape estimation. In addition, the coherent process can generate false images due to speckle noise or the grating-lobe effect, and its computational cost severely depends on the imaging area and often becomes significantly large as it includes an entire portion of the background concrete media.

1) RPM Image Prior for ROI Limitation: To overcome the above difficulties associated with coherent-based radar imaging, the RPM was developed and demonstrated in the NDT observation model [10]. It focuses on the boundary extraction of buried objects, where discrete observation points, named range points, are accurately converted to their corresponding scattering centers on the boundary. Here, assuming a typical NDT scenario, each object (e.g., air cavity, metallic rust, or other cracks) is sparsely distributed in the homogeneous background media (i.e., concrete media). Under this assumption, the ROI can be determined by the proximity area of scattering centers reconstructed by the RPM method [8].

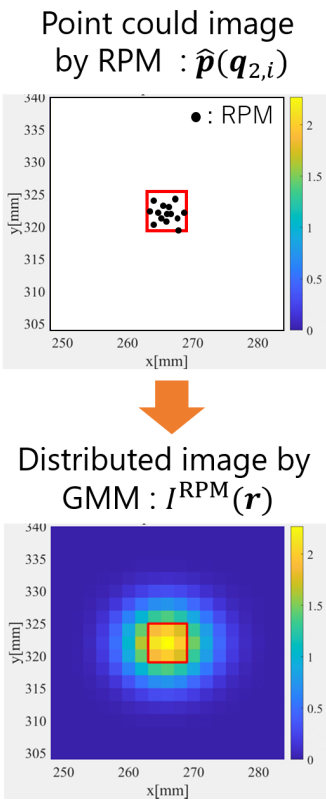

Fig. 2. Converting from RPM point cloud image to 2-D distributed Gaussian kernel image.

Here, we briefly describe the principle of the RPM method as follows. As described in Section II-A, discrete data points (known as range points), $\boldsymbol{q}_{1,i}$ and $\boldsymbol{q}_{2,i}$, are observed at each sensor location. RPM then converts the range point, $\boldsymbol{q}_{2,i}$, to the corresponding scattering center $\boldsymbol{p}(\boldsymbol{q}_{2,i})$ as follows:

$$\hat{\boldsymbol{p}}(\boldsymbol{q}_{2,i}) = \arg\max_{\boldsymbol{p}_{i,k}^{\text{int}}} \sum_j |s(\boldsymbol{q}_{2,j})| \exp\left\{-\frac{\|\boldsymbol{r}_{2,i} - \boldsymbol{r}_{2,j}\|^2}{2\sigma_X^2}\right\} \times \exp\left\{-\frac{\|\boldsymbol{p}_{i,j}^{\text{int}} - \boldsymbol{p}_{i,k}^{\text{int}}\|^2}{2\sigma_r^2}\right\} \exp\left\{-\frac{|R_{2,m} - R_{2,j}|^2}{2\sigma_R^2}\right\}. \tag{8}$$

Here $\boldsymbol{p}_{i,j}^{\text{int}}$ is the intersection point among orbits in the propagation paths determined by $\boldsymbol{q}_{2,i}$ and $\boldsymbol{q}_{2,j}$, which are determined by the dielectric constants of the background media. σ_X and σ_r are constant parameters. Specifically, σ_r should be determined using a spatial profile of the accumulated intersection points, which could be determined by an aperture angle, and σ_D should be set with a couple of sensor intervals, more details are described in [7]. A number of studies have demonstrated that RPM can accurately determine the scattering center points on the object boundary, even if the received signal includes multiple reflections. Moreover, the distribution of range points can become significantly complicated leading to a heavily interfered situation. Furthermore, since the conversion process is incoherently done, it could prevent unnecessary responses due to sidelobes or speckles. The RPM methodology is simple, and the computational time it requires depends on the number of targets rather than the scale of the background media. This method is also promising for sparsely distributed profiles assumed in NDT models. Note that, if the observation area Ω_S fully surrounds each object buried in concrete media, it is possible to reconstruct an entire area of the object surface, providing a complete ROI boundary. However, in a typical NDT model, Ω_S is significantly limited to the area in front of the concrete surface (Fig. 1), and the radar-based ROI could be difficult to estimate the entire boundary of each ROI.

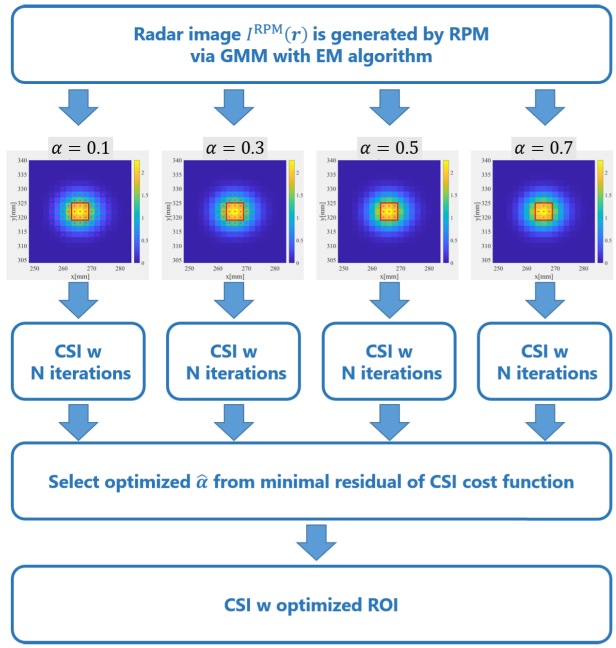

Fig. 3. Conceptual illustration for optimizing the threshold α from the Gaussian kernel-based radar image $I^{\text{RPM}}(\boldsymbol{r})$ and the processing of the proposed method.

2) ROI Optimization by Incorporating RPM and CSI: A procedure for how the proposed method exploits a group of scattering center points reconstructed by the RPM as the prior estimation of the ROI is provided as follows. To convert the RPM point-could image to a distributed image as $I^{\text{RPM}}(\boldsymbol{r})$, the following 2-D GMM is introduced as follows:

$$I^{\text{RPM}}(\boldsymbol{r}) = \sum_{k=1}^{N} \pi_k \mathcal{N}(\boldsymbol{r} \mid \boldsymbol{\mu}_k, \boldsymbol{\Sigma}_k) = \sum_{k=1}^{N} \frac{\pi_k}{\sqrt{(2\pi)^m |\boldsymbol{\Sigma}_k|}} \times \exp\left\{-\frac{1}{2}(\boldsymbol{r} - \boldsymbol{\mu}_k)^{\text{T}} \boldsymbol{\Sigma}^{-1} (\boldsymbol{r} - \boldsymbol{\mu}_k)\right\} \tag{9}$$

where N is the number of clusters. π_k, $\boldsymbol{\mu}_k$, and $\boldsymbol{\Sigma}_k$ denote weights, mean vector, and covariance matrix, respectively, for kth cluster. The parameters $\pi_k, \boldsymbol{\mu}_k, \boldsymbol{\Sigma}_k$ could be simultaneously optimized in the maximum likelihood procedure using the expectation maximization (EM) algorithm [42]. Fig. 2 shows the conversion of the RPM point-cloud image to the 2-D distributed image using the GMM model.

To determine the ROI area, the profile of $I_{\mathrm{BI}}^{\mathrm{RPM}}(\boldsymbol{r})$ is defined as binary expression

$$I_{\mathrm{BI}}^{\mathrm{RPM}}(\boldsymbol{r};\alpha) \equiv \begin{cases} 1, & \left(I^{\mathrm{RPM}}(\boldsymbol{r}) \geq \alpha \max_{\boldsymbol{r}} \ I^{\mathrm{RPM}}(\boldsymbol{r})\right) \\ 0, & (\text{otherwise}) \end{cases} \tag{10}$$

where α denotes the threshold. Then, the ROI is redefined as follows:

$$\tilde{\Omega}(\boldsymbol{r};\alpha) = \left\{\boldsymbol{r} \middle| I_{\mathrm{BI}}^{\mathrm{RPM}}(\boldsymbol{r};\alpha) > 0\right\}. \tag{11}$$

The selected ROI is determined by the value of the threshold of α. The proposed method optimizes the α by the following equation to obtain an appropriate ROI:

$$\hat{\alpha} = \arg\min_{\alpha} \ \left\{\tilde{F}^{\mathrm{S}}\left(w_{j,k}(\boldsymbol{r});\tilde{\Omega}(\boldsymbol{r};\alpha)\right) + \tilde{F}^{\mathrm{D}}\left(w_{j,k}(\boldsymbol{r}), O_j(\boldsymbol{r});\tilde{\Omega}(\boldsymbol{r};\alpha)\right)\right\} \tag{12}$$

where

$$\tilde{F}^{S}(w_{j,k}(\boldsymbol{r});\tilde{\Omega}(\boldsymbol{r};\alpha)) \equiv \frac{1}{J}\sum_j \frac{\sum_k \left\| E_{j,k}^{\mathrm{S}}(\boldsymbol{r}_r) - k_{\mathrm{b}}^2 \int_{\tilde{\Omega}(\boldsymbol{r};\alpha)} G_j^{\mathrm{b}}(\boldsymbol{r}_r,\boldsymbol{r}') w_{j,k}(\boldsymbol{r}') d\boldsymbol{r}' \right\|_{\Omega_{\mathrm{S}}}^2}{\sum_k \left\| E_{j,k}^{\mathrm{S}}(\boldsymbol{r}_r) \right\|_{\Omega_{\mathrm{S}}}^2} \tag{13}$$

$$\tilde{F}^{\mathrm{D}}\left(w_{j,k}(\boldsymbol{r}), O_j(\boldsymbol{r});\tilde{\Omega}(\boldsymbol{r};\alpha)\right) \equiv \frac{1}{J}\sum_j \frac{\sum_k \left\| O_j(\boldsymbol{r}) E_{j,k}^{\mathrm{T}}(\boldsymbol{r}) - w_{j,k}(\boldsymbol{r}) \right\|_{\tilde{\Omega}(\boldsymbol{r};\alpha)}^2}{\sum_k \left\| O_j(\boldsymbol{r}) E_{j,k}^{\mathrm{I}}(\boldsymbol{r}) \right\|_{\tilde{\Omega}(\boldsymbol{r};\alpha)}^2} \tag{14}$$

holds. Here, the residual of the cost function denoted as $\tilde{F}^{S}(w_{j,k}(\boldsymbol{r});\tilde{\Omega}(\boldsymbol{r};\alpha))$ and $\tilde{F}^{\mathrm{D}}(w_{j,k}(\boldsymbol{r}), O_j(\boldsymbol{r});\tilde{\Omega}(\boldsymbol{r};\alpha))$ is assessed in the early stage of the iteration step in the CSI as N_{init} steps, to assess the dependency of the convergence speed as to α, because it is assumed that if an appropriate ROI is selected, the cost function would rapidly decrease. This algorithm is based on the justification that if the ROI is correctly selected, the CSI will reconstruct an accurate complex permittivity profile, implying that the residual of the CSI's cost function in (5) will also become small. According to this inference, if the residual of the cost function is minimal, the selected ROI will be close to the true ROI, and the threshold parameter α will be optimized by minimizing the cost function in the CSI. Fig. 3 shows a schematic of how to use the CSI cost function to optimize the threshold of the RPM point-could image.

Finally, the CSI with a limited ROI denoted as $\tilde{\Omega}(\boldsymbol{r};\alpha)$ is performed. Because the targets (e.g., air cavity or metallic pipe) are significantly small compared with the background media, this process reduces the number of unknowns to be estimated in the actual NDT for transportation infrastructure. The proposed method can then improve accuracy not only for the ROI estimate but also for dielectric profile reconstruction using the CSI scheme.

III. Performance Evaluation via FDTD Numerical Analysis

A. Numerical Setting

In this section, the reconstruction performance with quantitative evaluation based on 2-D FDTD numerical data is demonstrated. Fig. 4 shows that the target and array configuration assumed in this numerical test is the specific NDT model. The 27 sets of transmitting and receiving antennas are linearly arranged with 30 mm equal spacing, 158 mm from the concrete surface. All the combination data for the transmitting and receiving antennas are exploited for the reconstruction; hence, multistatic observation is assumed. The transmitted signal is assumed to be an ultrawideband pulse formed by a Gaussian-modulated pulse with a center frequency of 2.45 GHz and a bandwidth of 2.7 GHz. Point-form source and receiver are assumed in this simulation, for simplicity. The background media is constituted by a concrete material, and five different types of targets, such as air cavity and different types of metallic rusts, are buried in the concrete media. The size and dielectric properties of the concrete media and each target [11] are summarized in Table I. In this simulation, the dimension and dielectric property of the background concrete media is given. Note that, the literature [11] demonstrated complex permittivity of concrete media or each object did not have a significant frequency dependency for this frequency band, and in this case, a non-dispersive media or object is assumed in the FDTD data generation. In both CSI, the cell size for the forward (FDTD) and inverse solutions is 2 mm square. In addition, the FDTD method numerically provides Green's function of the background media, which is concrete media without an object. The total number of unknowns, including the concrete (background) media, is 40 240. The center wavelength and the range resolution in the background media are approximately estimated as 46 and 42 mm, respectively. Note that, any target size assumed is less than a wavelength or the range resolution.

TABLE I
Dielectric Properties and Size of Background Medium and Each Target

	ϵ_r	σ [S/m]	size [mm]
Background medium	7.0	0.001	1006×360
Black rust (#1)	12.58	1.31	6×6
Salt rust (#2)	5.33	0.29	10×6
Hydrated black rust (#3)	11.28	1.14	22×4
Air cavity (#4)	1	0	8×6
Red rust (#5)	8.42	0.57	6×6

B. Initial Results of RPM Image

First, we present the results of RPM imaging and the 2-D Gaussian kernel-based distribution image as $I^{\mathrm{RPM}}(\boldsymbol{r})$, which is described in Section II-C1. The scattering center points are estimated using RPM and the distributed image generated in (9), and the extracted ROI using the specific threshold, where each RPM parameter is set as σ_X 2.0 mm and $\sigma_r = 1.0$ mm, is shown in Fig. 5. As shown in Fig. 5, the RPM accurately reconstructs the location of the scattering center on each target boundary, which cannot be obtained by conventional coherent integration methods such as SAR or RMA due to speckle noise or grating lobe, has been

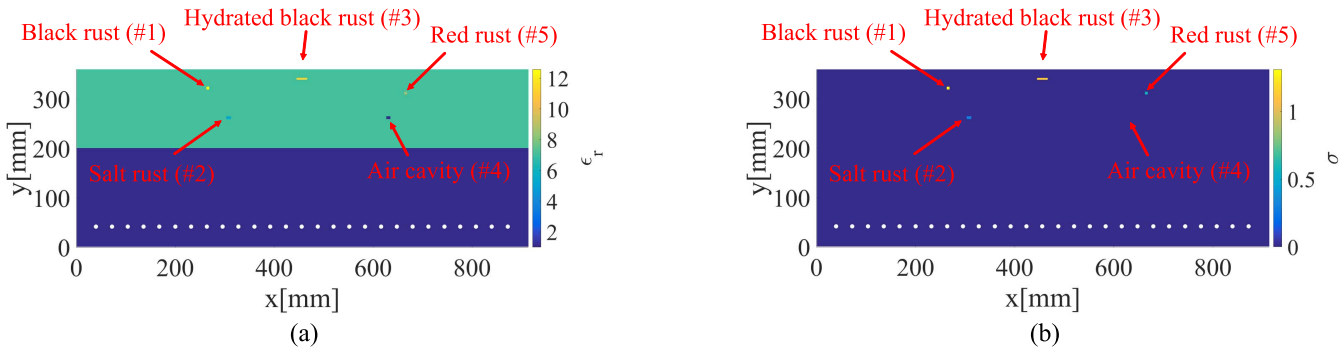

Fig. 4. True profiles in numerical simulation model. (a) Relative permittivity. (b) Conductivity.

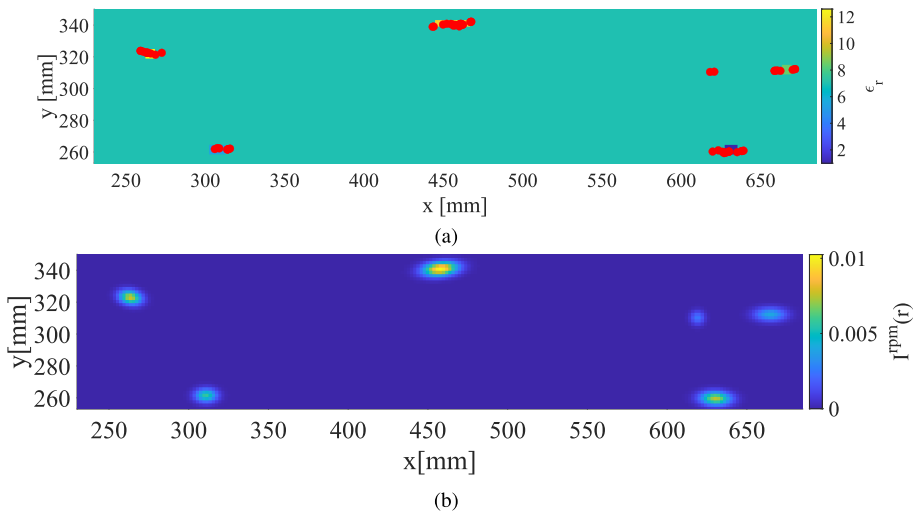

Fig. 5. Point cloud (a) RPM image $\hat{\boldsymbol{p}}(\boldsymbol{q}_{2,i})$ and (b) Gauss kernel conversion image $I^{\mathrm{RPM}}(\boldsymbol{r})$.

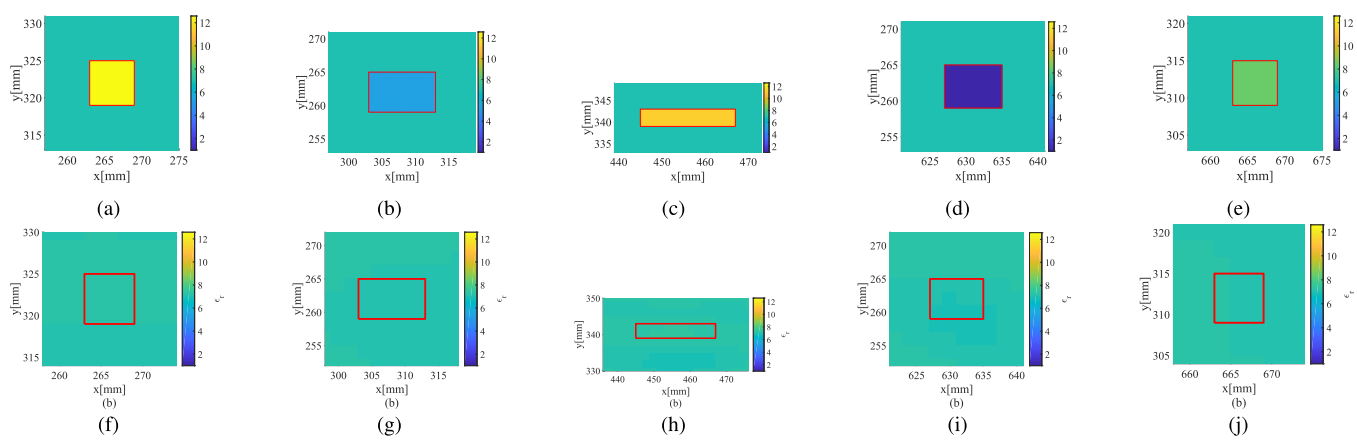

Fig. 6. Reconstruction profiles by DBIM method in relative permittivity. Magenta dots denote the selected ROI. Color scale denotes a relative permittivity. (a)–(e) Original profile (first line). (f)–(j) DBIM without ROI limitation (second line).

demonstrated in a similar test in [8]. These figures also indicate that we must determine the appropriate threshold α to extract accurate ROI for post CSI processing.

C. Reconstruction Results for Relative Permittivity and Conductivity

Next, we investigate CSI-based reconstruction methods, described in Section II-B, namely, with or without ROI limitation. The maximum iteration number of the CSI was set to 4096, and single-frequency data as 3.68 GHz was used. Figs. 6 and 7 show the original profile of each target for relative permittivity and conductivity, respectively. At first, for the method comparison of other promising inversion scheme, Figs. 6(f)–(i) and 7(f)–(i) shows the reconstruction of the DBIM, where five different frequency data (1.15, 1.61, 2.53, 3.22, 3.68) GHz are used with the maximum iteration number set to 100, and the conjugate gradient least square (CGLS) algorithm is used to update the $\chi_j(\mathbf{r})$, the

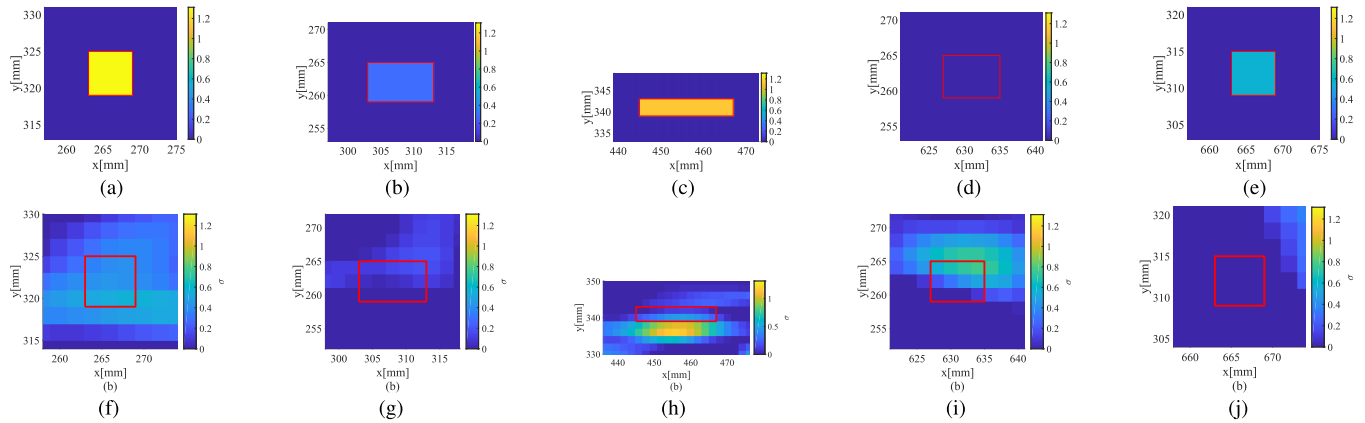

Fig. 7. Reconstruction profiles by DBIM method in conductivity. Magenta dots denote the selected ROI. Color scale denotes a conductivity (S/m). (a)–(e) Original profile (first line). (f)–(j) DBIM without ROI limitation (second line).

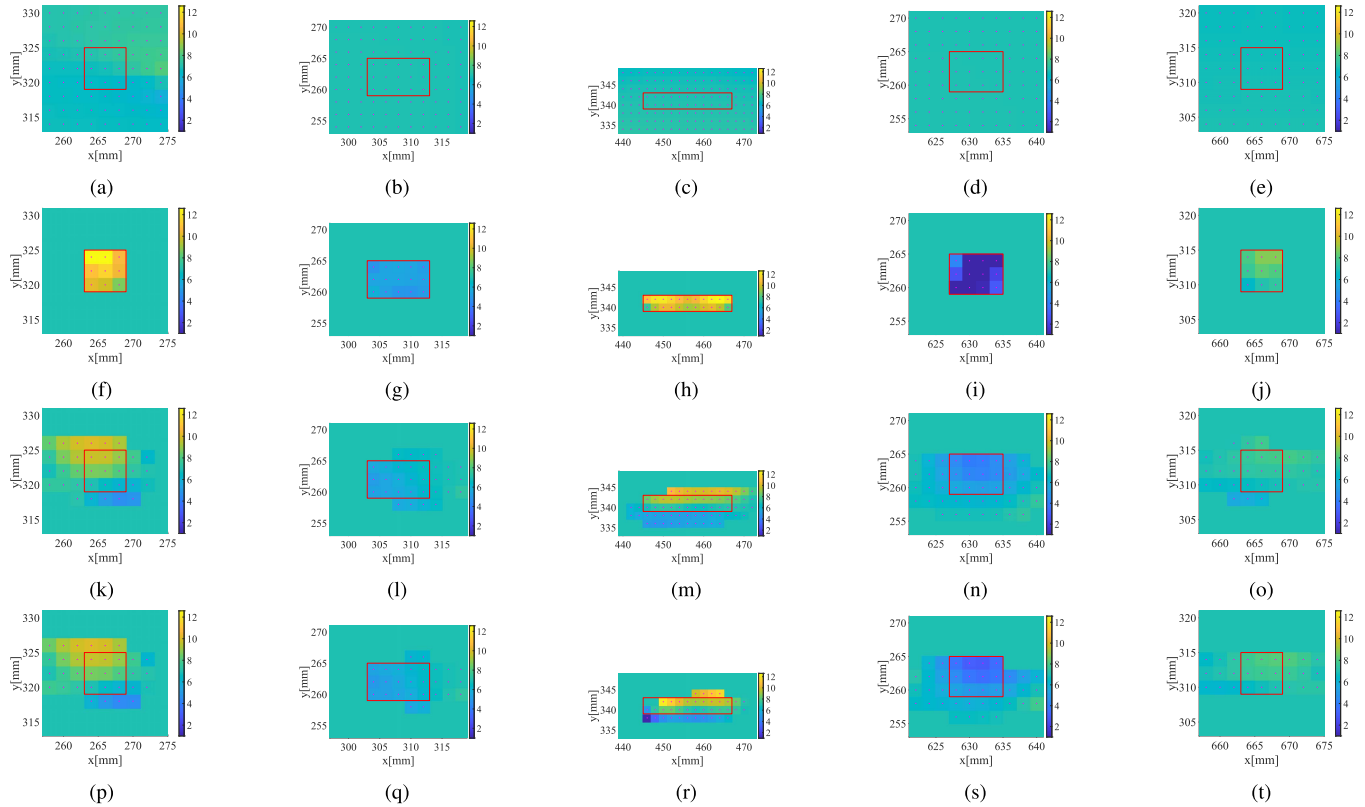

Fig. 8. Reconstruction results by for each CSI-based method in relative permittivity. Magenta dots denote the selected ROI. Color scale denotes a relative permittivity. (a)–(e) CSI without ROI limitation (first line). (f)–(j) CSI with true ROI limitation (second line). (k)–(o) CSI with initial ROI limitation (third line). (p)–(t): CSI with optimized ROI limitation (proposed method) (fourth line).

details of which have been published in some studies such as [15]. These results demonstrate that the original DBIM (without ROI limitation) method could not provide an accurate profile of each target, most of which are similar to background media. This is because the number of unknowns is significantly larger than that of data samples, and note that the DBIM requires a forward solver calculation in each iteration step, which requires more computational cost than that required in the CSI.

Furthermore, Figs. 8 and 9 show the results using the CSI-based reconstruction, where the ROI is not limited or limited by the true ROI, the initial ROI, or the optimized ROI. Here, we called the case as the initial ROI, where the ROI threshold is fixed sufficiently lower. First, in focusing on the case that the ROI is not limited [Figs. 8(a)–(e) and 9(a)–(e)], but is given as a whole area of the background, the CSI-based reconstruction scheme does not provide meaningful results, which is far from the original profile, this is because the number of ROI including the whole background area goes to 40 240, which is quite larger than that of data as 729 (27×27). On the contrary, if we give the true ROI, the CSI could provide quite an accurate dielectric profile both in

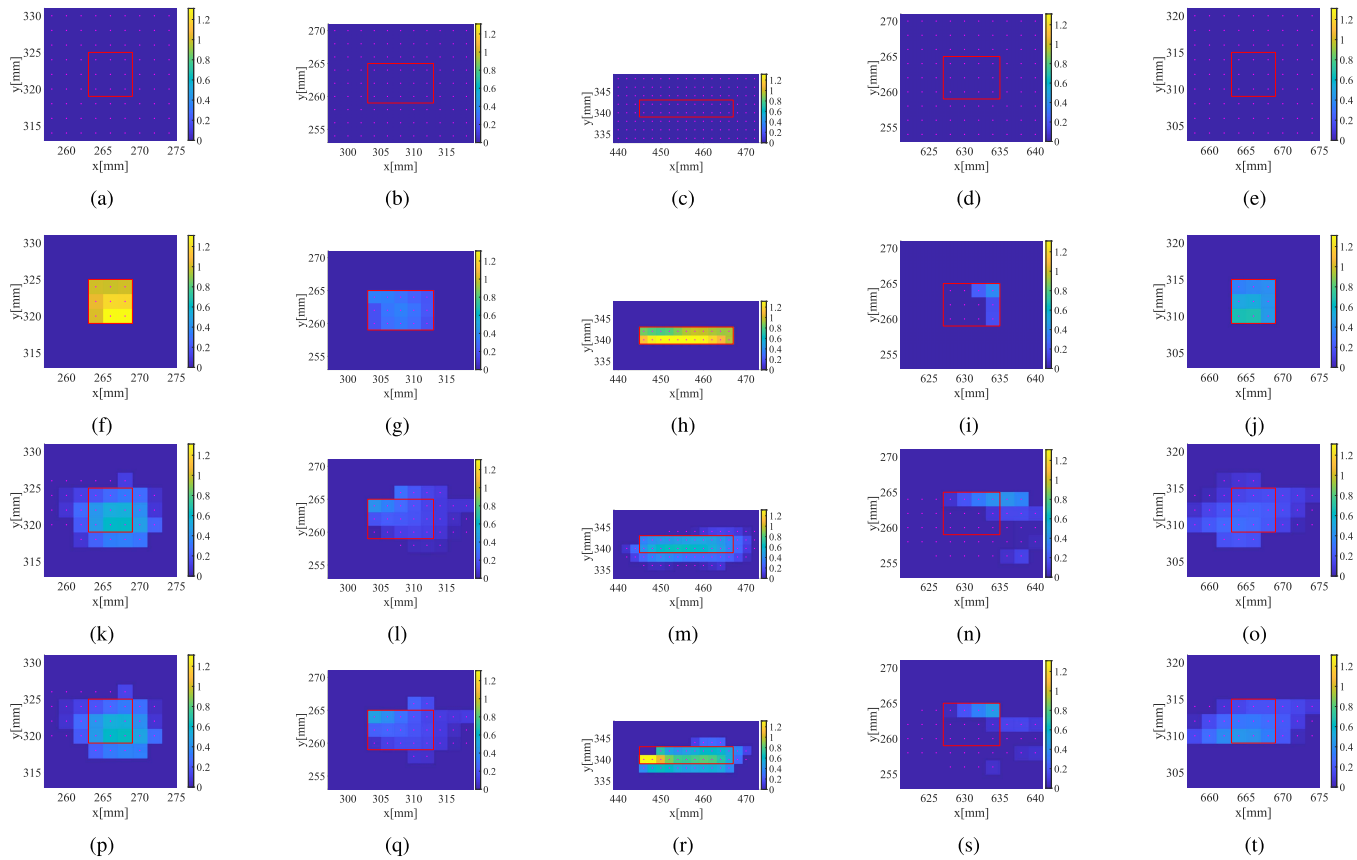

Fig. 9. Reconstruction results by for each CSI-based method in relative permittivity. Magenta dots denote the selected ROI. Color scale denotes a conductivity with a unit of S/m. (a)–(e) CSI without ROI limitation (first line). (f)–(j) CSI with true ROI limitation (second line). (k)–(o) CSI with initial ROI limitation (third line). (p)–(t) CSI with optimized ROI limitation (proposed method) (fourth line).

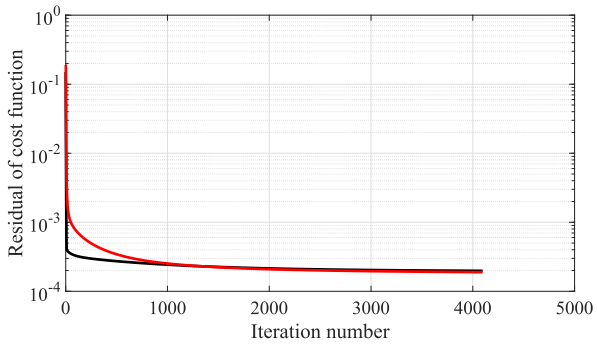

Fig. 10. Transition of cost function versus iteration steps in each case. Black and red curves denote the residuals of the cost function of the CSI in the case for with true and optimized ROI cases, respectively, in the case of Section III-C.

TABLE II

TOTAL COMPUTATIONAL TIME FOR RECONSTRUCTION BY EACH METHOD IN THE CASE OF SECTION III-C

DBIM w/o ROI limit	1.00×10^6 s
CSI w/o ROI limit	1.46×10^6 s
CSI w true ROI	73 s
CSI w initial ROI	127 s
CSI w optimized ROI	159 s

relative permittivity and conductivity as shown in Figs. 8(f)–(j) and 9(f)–(j), demonstrating that our proposed scheme is much effective to reconstruct a sparsely distributed target. This is because the size of each object is significantly smaller than the wavelength, and thus, a small number of unknowns would be allocated, which alleviates an ill-posedness. However, the ROI, that is, the shape or location of each object, would not be provided as prior knowledge when considering the realistic NDT operation, so the ROI estimation is required.

The results in Figs. 8(k)–(o) and 9(k)–(o) show the results using the initial ROI. Also, in Figs. 8(p)–(t) and 9(p)–(t) show the CSI-based reconstruction, where the ROI is optimized using the algorithm described in Section II-C2. $N_{\text{init}} = 20$ is set to determine the threshold α in (12). Here, the number of unknown cells is downsized from 40 240 (whole area of background) to to 246 (99.4% reduced) by the ROI optimization of the proposed method. First, the CSI result with ROI limitation provides a more accurate dielectric profile than the original CSI, which is without ROI limitation because

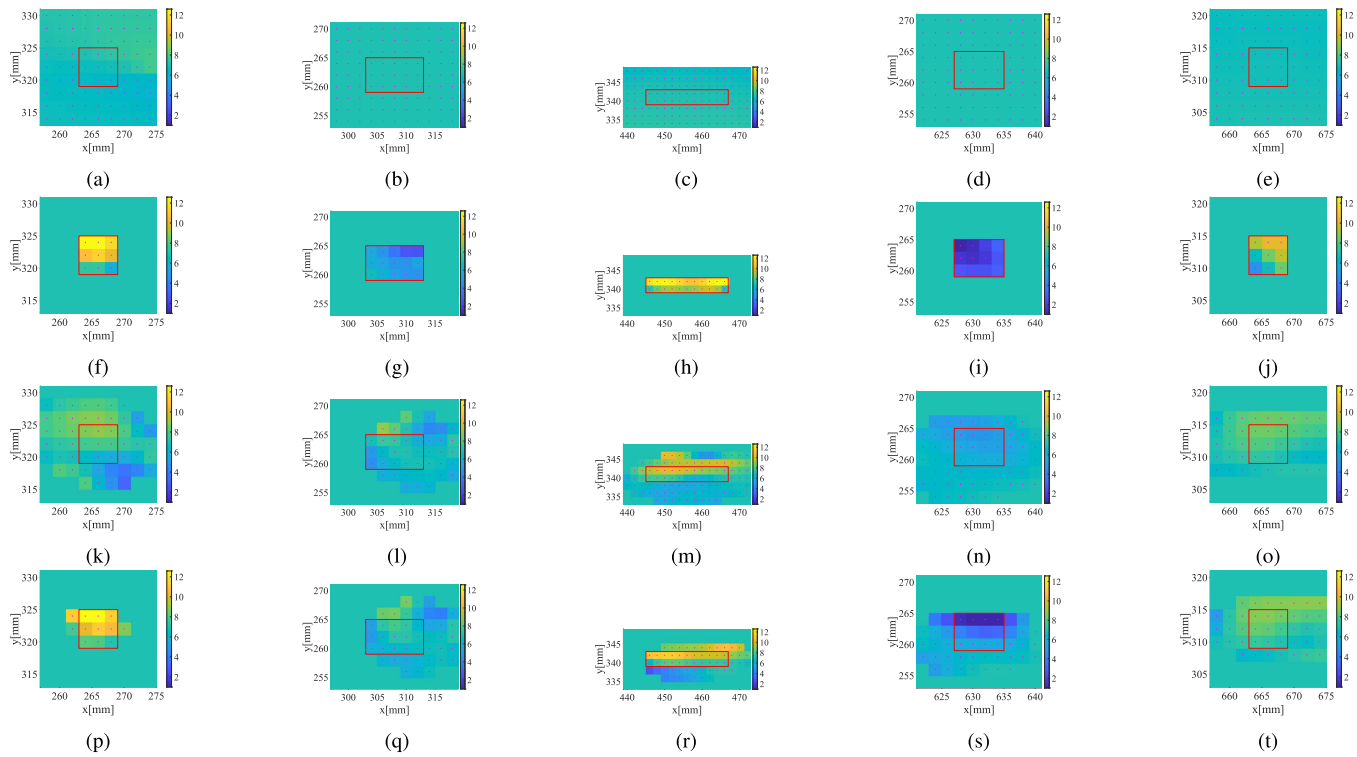

Fig. 11. Reconstruction results by CSI-based methods with true and optimized ROI limitations in relative permittivity at the case of SNR is 20 dB. Magenta dots denote the selected ROI. Color scale denotes a relative permittivity. (a)–(e) CSI without ROI limitation (first line). (f)–(j) CSI with true ROI limitation (second line). (k)–(o) CSI with initial ROI limitation (third line). (p)–(t): CSI with optimized ROI limitation (proposed method) (fourth line).

TABLE III

RMSE_ϵ AND RMSE_σ FOR RECONSTRUCTION RESULTS OF (ϵ_r, σ [S/m]) BY EACH CSI ALGORITHM IN THE CASE OF SECTION III-C

	DBIM w/o ROI limit	CSI w/o ROI limit	CSI w true ROI	CSI w initial ROI	CSI w optimized ROI
#1	(5.38, 0.85)	(1.96,0.44)	(0.73, 0.11)	(1.77, 0.36)	(1.80, 0.31)
#2	(1.75, 0.22)	(0.64,0.11)	(0.12, 0.03)	(0.36, 0.07)	(0.32, 0.06)
#3	(3.96, 0.92)	(1.73,0.46)	(0.63, 0.09)	(1.72, 0.28)	(1.66, 0.28)
#4	(5.99, 0.35)	(2.18,0.00)	(0.46, 0.05)	(1.47, 0.09)	(1.31, 0.07)
#5	(1.29, 0.57)	(0.57,0.19)	(0.31, 0.05)	(0.50, 0.14)	(0.43, 0.12)

the number of unknowns is remarkably reduced. Second, compared with the initial estimate, the ROI optimizing scheme provides a more accurate ROI. However, the reconstruction results still have errors in the dielectric profile and ROI because the Gaussian kernel-distributed image could not necessarily express the actual ROI because of the RPM imaging limitations. Nonetheless, these results by the proposed scheme have significance, because the inverse problem model assumed in this study is extremely difficult, in terms of ill-posed conditions or limitations of illumination angles, and each target has a size within a wavelength, the shape of which could not be accurately determined by the traditional radar approach, such as SAR. Furthermore, Table II summarizes the computational time for the inversion in each method, using Intel(R) Xeon(R) CPU E5-2620 2.4 GHz and 128 GB RAM. This table also demonstrates that the proposed method considerably reduces the computational cost, compared with the original DBIM or CSI, by reducing the number of unknowns. In addition, the transition of the residual of the cost function to show convergence in each case is shown in Fig. 10. When we obtain the true ROI, the cost function rapidly decreases compared to the case using the estimated ROI in the proposed method. This fact is the basis of the proposed method for optimizing the ROI selection threshold parameter α in a few iteration steps by referring to the residual of the cost function.

Table III summarizes the quantitative error analysis in terms of the root mean square error (RMSE) for the relative permittivity and conductivity for each target defined as follows:

$$\mathrm{RMSE}_\epsilon = \sqrt{\frac{1}{N}\sum_{i=1}^{N}|\epsilon^{\mathrm{true}}(\boldsymbol{r}_i) - \epsilon^{\mathrm{est}}(\boldsymbol{r}_i)|^2} \tag{15}$$

$$\mathrm{RMSE}_\sigma = \sqrt{\frac{1}{N}\sum_{i=1}^{N}|\sigma^{\mathrm{true}}(\boldsymbol{r}_i) - \sigma^{\mathrm{est}}(\boldsymbol{r}_i)|^2} \tag{16}$$

where $\epsilon^{\mathrm{true}}(\boldsymbol{r}_i)$ and $\epsilon^{\mathrm{est}}(\boldsymbol{r}_i)$ denote the original and reconstructed relative permittivities at the position on $\boldsymbol{r}_i$, respectively. $\sigma^{\mathrm{true}}(\boldsymbol{r}_i)$ and $\sigma^{\mathrm{est}}(\boldsymbol{r}_i)$ are the conductivity, which is defined in the same way as relative permittivity. N denotes

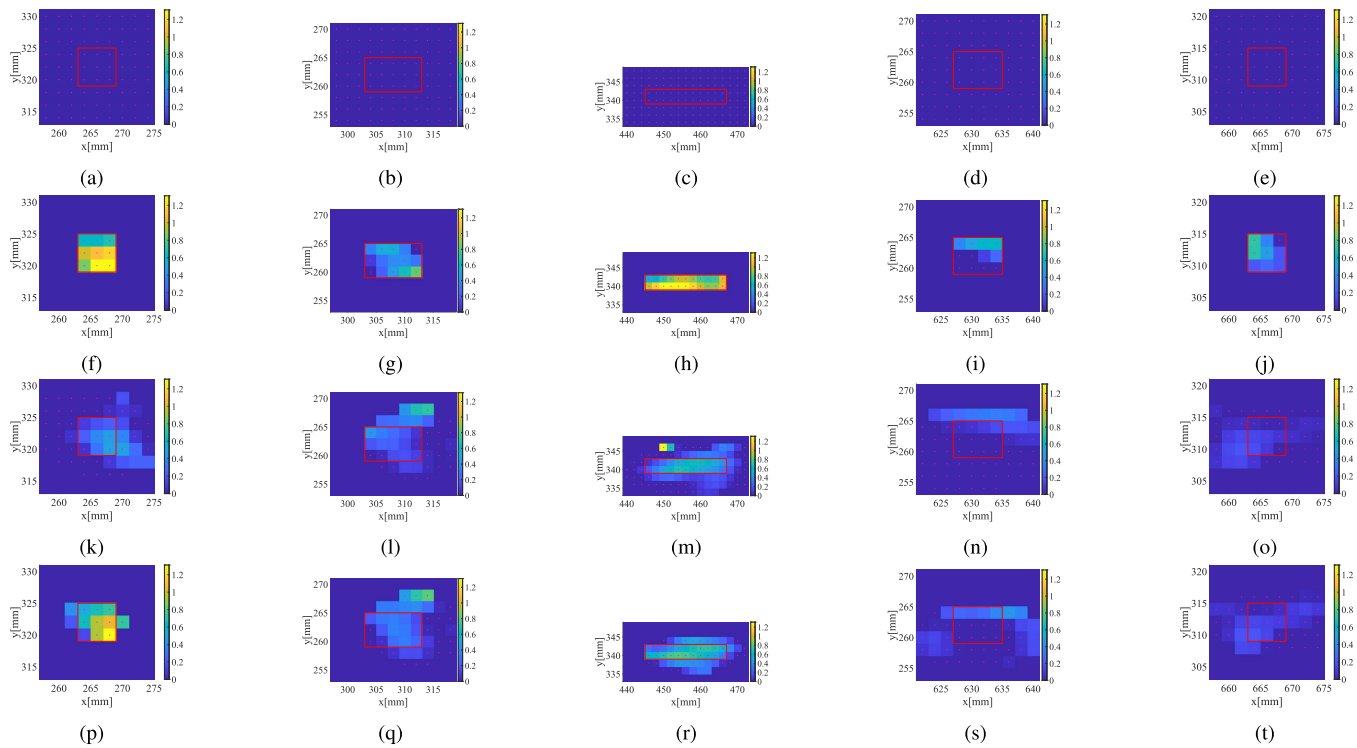

Fig. 12. Reconstruction results by CSI-based methods with true and optimized ROI limitations in conductivity at the case of SNR is 20 dB. Magenta dots denote the selected ROI. Color scale denotes a conductivity with a unit of S/m. (a)–(e) CSI without ROI limitation (first line). (f)–(j) CSI with true ROI limitation (second line). (k)–(o) CSI with initial ROI limitation (third line). (p)–(t) CSI with optimized ROI limitation (proposed method) (fourth line).

the number of cells allocated to each area (Fig. 8), including the actual ROI. In addition, quantitatively validate the ROI updating performance, the relative errors for ROI of the ith object is introduced as follows:

$$\mathrm{Err}_{\Omega_{\mathrm{D},i}} = \frac{\iint \left|\eta_i^{\mathrm{true}}(\boldsymbol{r}) - \eta_i^{\mathrm{est}}(\boldsymbol{r})\right| d\boldsymbol{r}}{\iint \left|\eta_i^{\mathrm{true}}(\boldsymbol{r})\right| d\boldsymbol{r}} \tag{17}$$

where $\eta_i^{\mathrm{true}}(\boldsymbol{r})$ and $\eta_i^{\mathrm{est}}(\boldsymbol{r})$ are defined as follows:

$$\eta_i^{\mathrm{true}}(\boldsymbol{r}) = \begin{cases} 1, & \left(\boldsymbol{r} \in \Omega_{\mathrm{D},i}^{\mathrm{true}}\right) \\ 0, & (\text{otherwise}) \end{cases} \tag{18}$$

$$\eta_i^{\mathrm{est}}(\boldsymbol{r}) = \begin{cases} 1, & \left(\boldsymbol{r} \in \Omega_{\mathrm{D},i}^{\mathrm{est}}\right) \\ 0, & (\text{otherwise}) \end{cases} \tag{19}$$

where $\Omega_{\mathrm{D},i}^{\mathrm{true}}$ and $\Omega_{\mathrm{D},i}^{\mathrm{est}}$ denote the true and estimated ROI for ith object, respectively. Table IV shows the relative errors $\mathrm{Err}_{\Omega_{\mathrm{D},i}}$ in each object for the reconstructed ROI in the proposed method. This table shows that the proposed method, CSI with ROI limitation, efficiently enhances reconstruction accuracy for both relative permittivity and conductivity compared to the original CSI without ROI limitation. Furthermore, as compared to the initial ROI, ROI optimization provides a significantly more accurate target shape and location, which would be difficult to achieve using the conventional radar imaging technique in such a frequency band.

D. Sensitivity to Additive Noise

In this section, we investigate the sensitivity of additive random noise in each method. In the time domain, Gaussian white noise is directly added to the scattered electric field.

TABLE IV

$\mathrm{Err}_{\Omega_{\mathrm{D},i}}$ FOR EACH TARGET IN THE CASE OF SECTION III-C

Target (Area [mm^2])	CSI w initial ROI	CSI w optimized ROI
#1 (36)	3.22	3.11
#2 (60)	1.20	0.93
#3 (88)	2.09	0.95
#4 (48)	3.58	2.75
#5 (36)	3.56	2.56

TABLE V

RMSE_ϵ AND RMSE_σ FOR RECONSTRUCTION RESULTS OF (ϵ_r, σ [S/m]) AT THE CASE OF SNR IS 20 dB

	CSI w/o ROI limit	CSI w true ROI	CSI w init.ROI	CSI w opt. ROI
#1	(1.98,0.44)	(1.16, 0.15)	(1.97,0.36)	(1.14,0.23)
#2	(0.65,0.11)	(0.45, 0.09)	(0.82,0.14)	(0.84,0.15)
#3	(1.74,0.46)	(0.81, 0.12)	(1.72,0.32)	(1.54,0.28)
#4	(2.18,0.00)	(0.52, 0.12)	(1.77,0.10)	(1.48,0.10)
#5	(0.58,0.19)	(0.59, 0.10)	(0.57,0.17)	(0.68,0.17)

The signal-to-noise ratio (SNR) is defined as the time domain ratio of maximum signal power to the noise variance. Here, the case of 20 dB SNR is investigated, which is available in a realistic scenario, as in [10]. The reconstruction results for each target demonstrate that the proposed method maintains its reconstruction accuracy in this scenario and is shown in Figs. 11 and 12. The normalized RMSE (NRMSE) for relative permittivity and conductivity and the relative errors for the selected ROI are summarized in Tables V and VI, respectively.

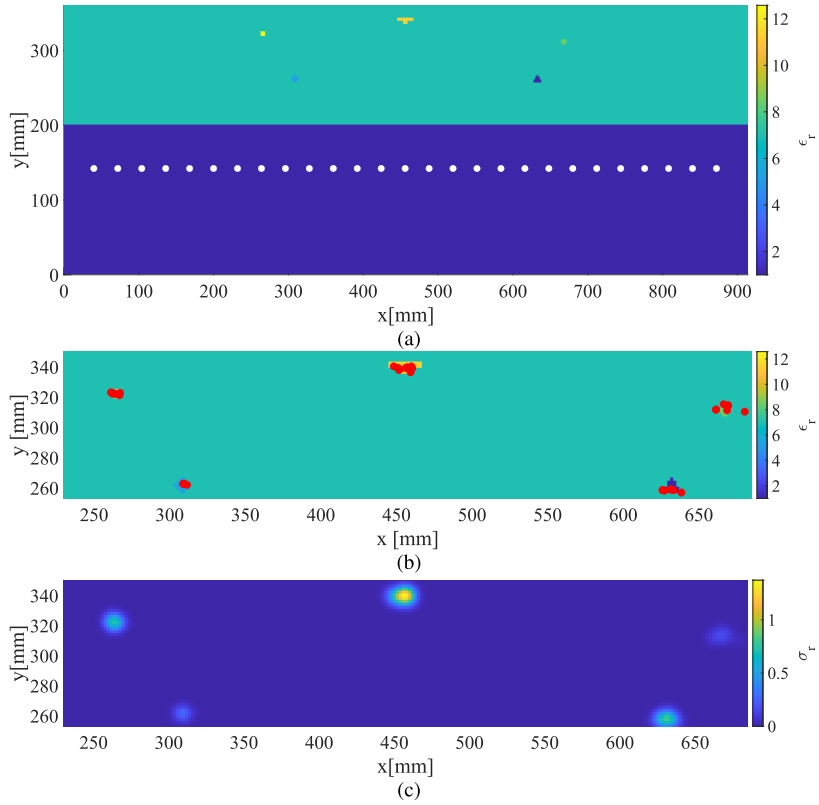

Fig. 13. Numerical model, point cloud RPM image $\hat{\boldsymbol{p}}(\boldsymbol{q}_{2,i})$ and the Gauss kernel conversion image $I^{\mathrm{RPM}}(\boldsymbol{r})$ in Section III-E. (a) Observation and target model. (b) RPM image $\hat{\boldsymbol{p}}(\boldsymbol{q}_{2,i})$. (c) Gauss kernel image $I^{\mathrm{RPM}}(\boldsymbol{r})$.

TABLE VI

$\mathrm{Err}_{\Omega_{\mathrm{D},i}}$ FOR EACH TARGET AT THE CASE OF SNR IS 20 dB

Target (Area [mm^2])	CSI w init. ROI	CSI w opt. ROI
#1 (36)	5.33	0.33
#2 (60)	2.13	2.13
#3 (88)	4.00	1.64
#4 (48)	6.58	3.25
#5 (36)	6.22	4.33

TABLE VII

RMSE_{ϵ} AND RMSE_{σ} OF THE RESULTS IN FIGS. 14 AND 15 USING THE MODEL IN FIG. 13

	CSI w/o ROI limit	CSI w true ROI	CSI w init. ROI	CSI w opt. ROI
#1	(1.95,0.44)	(0.66, 0.11)	(1.83,0.32)	(1.75,0.33)
#2	(0.61,0.11)	(0.12, 0.02)	(0.45,0.09)	(0.53, 0.09)
#3	(1.74,0.46)	(0.63, 0.08)	(1.96,0.30)	(1.88, 0.26)
#4	(2.18,0.00)	(0.33, 0.06)	(1.69,0.09)	(1.89, 0.03)
#5	(0.58,0.19)	(0.35, 0.05)	(0.67,0.16)	(0.70, 0.18)

While the RPM's ROI estimation is affected by random noise, its accuracy is maintained in a noisy scenario. This is because the RPM uses the range points extracted from the matched filter, which is the most noise-robust filter, and the RPM exploits all range points to reconstruct the scattering center for $\boldsymbol{q}_{2,i}$, which would contribute some averaging effect, its noise-robustness has been demonstrated in the detail in [7] and [8]. In addition, the reconstruction results of complex permittivity by the CSI-based method, are not significantly degraded compared with those obtained in the noise-free cases, because the CSI uses scattered data around the center frequency, which has the highest SNR level than other frequencies. These results demonstrate that our proposed method would work well in the actual noisy scenarios.

TABLE VIII

$\mathrm{RMSE}_{\Omega_{\mathrm{D},i}}$ [mm^2] FOR EACH TARGET IN FIG. 13 IN USING THE MODEL IN FIG. 13

Target (Area [mm^2])	CSI w init. ROI	CSI w opt. ROI
#1 (36)	4.33	4.11
#2 (72)	1.17	0.33
#3 (112)	1.57	1.57
#4 (68)	2.76	0.76
#5 (48)	4.92	0.83

E. Case in Highly Lossy Background and Complicated Shape Object

In this section, different observation conditions or object shapes are considered in numerical testing. The other numerical model assumed in this section is shown in Fig. 13. Because humid concrete media would cause rustic corrosion, we assumed more lossy background media by setting the

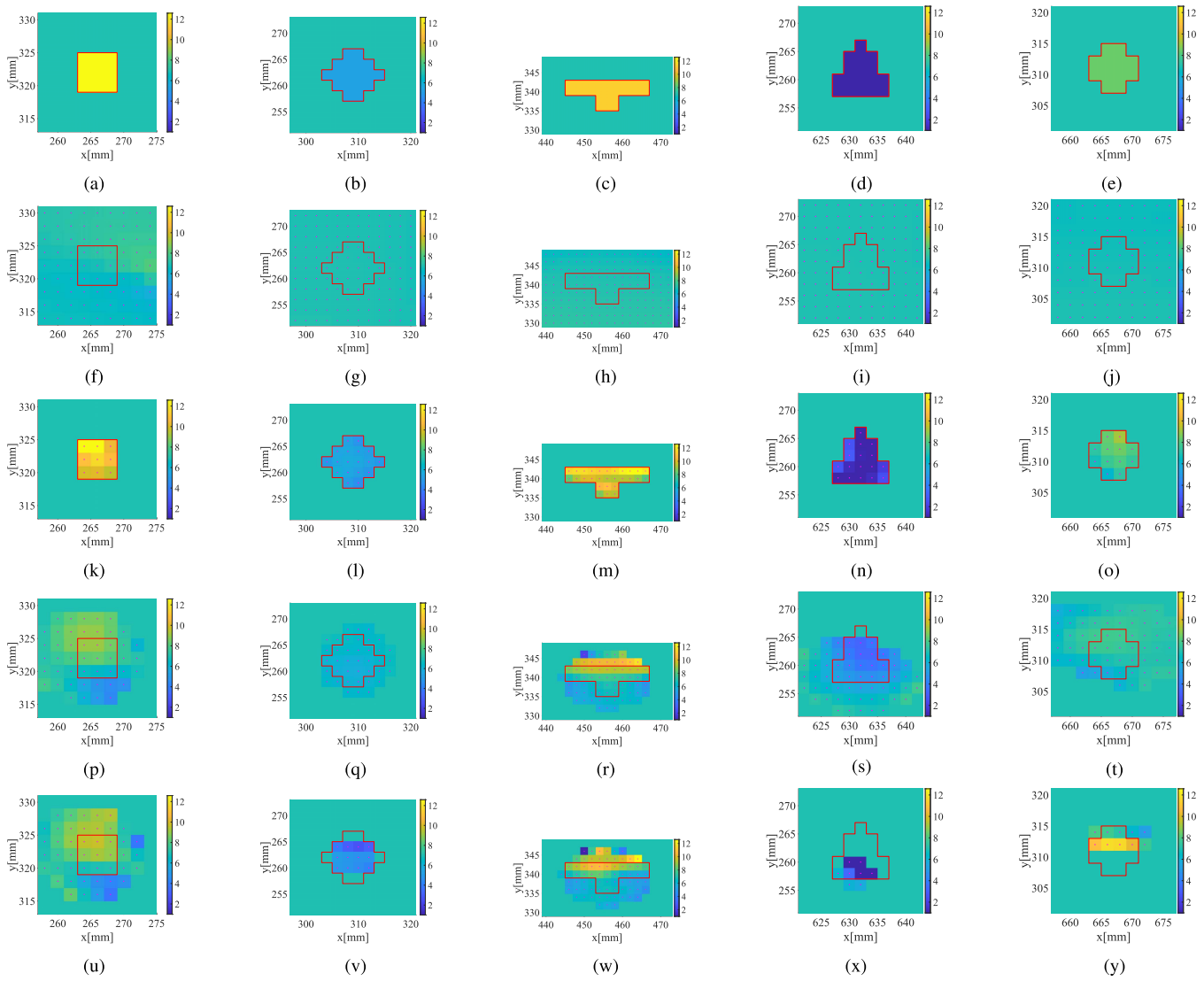

Fig. 14. Reconstruction results by CSI-based methods with or without ROI limitations in relative permittivity using the model in Fig. 13. Magenta dots denote the selected ROI. Color scale denotes a relative permittivity. (a)–(e) Original profile (first line). (f)–(j) CSI without ROI limitation (second line). (k)–(o) CSI with true ROI limitation (third line). (p)–(t) CSI with initial ROI limitation (fourth line). (u)–(y) CSI with optimized ROI limitation (proposed method) (fifth line).

conductivity to 0.01 m/S, which is ten times higher than in the previous case. In addition, to assess the influence of the sensor locations, we reset the positions of the observation sample to be closer to the surface of concrete media (Fig. 13). Furthermore, to consider off-grid object shapes, various types of irregular shapes, such as triangular, circle, hexagon, rectangular with notches, were assumed (Fig. 13). Other numerical setups such as cell size and induced current waveform, are the same as those in Section III-A. Fig. 13(b) and (c) denote the RPM reconstruction points and its generated distributed image by Gaussian kernel, and demonstrates that the RPM offers an accurate target area even in such complicated target shape. Figs. 14 and 15 show the reconstruction results for each object using the true, the initial, and the optimized ROI-based CSI method in relative permittivity and conductivity, respectively. The parameters in the CSI are set to the same used in the previous model. As shown in these figures, when we give the true ROI, the CSI offers accurate dielectric profiles in both permittivity and conductivity. Also, the proposed method, namely the CSI with the optimized ROI, provides a certain level of accuracy by limiting the ROI results and provides more accurate ROI, rather than those in the initial estimate. However, there are still non-negligible errors in the ROI estimation, especially for four targets, because the RPM could provide the scattering center points of the front side of the target boundary in this observation model, and its backside image could not be retrieved in such a model. Furthermore, in other target cases, Tables VII and VIII and denotes the NRMSE for the complex permittivity and the ROI reconstruction, and these results quantitatively demonstrate that our proposed method provides a certain level of accuracy, even in such extremely ill-posed conditions with no prior knowledge of the target location. Further investigations and upgrades of the ROI optimizing schemes should be needed to obtain a more accurate profile.

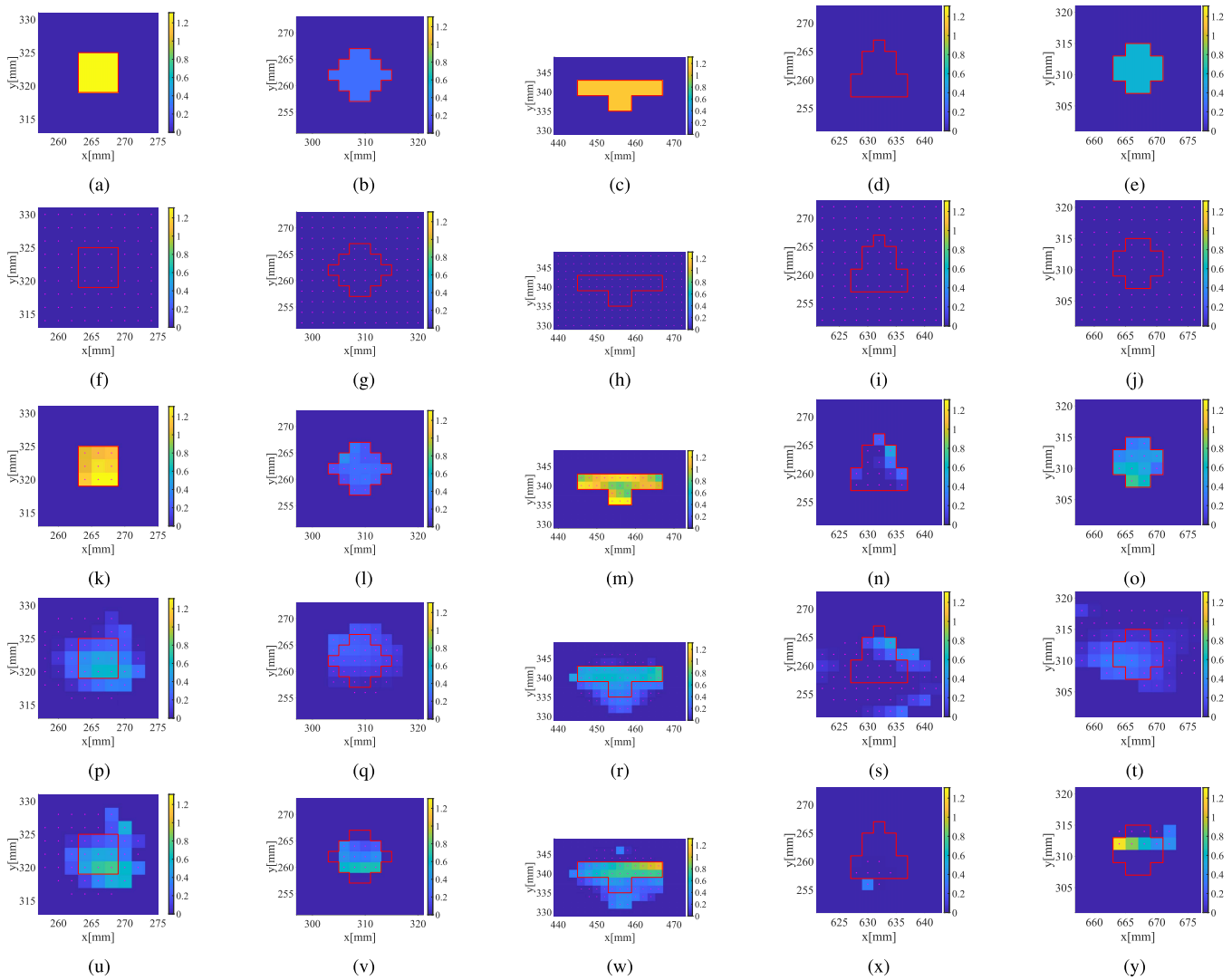

Fig. 15. Reconstruction results by CSI-based methods with or without ROI limitations in conductivity using the model in Fig. 13. Magenta dots denote the selected ROI. Color scale denotes a conductivity with a unit of S/m. (a)–(e) Original profile. (f)–(j) CSI without ROI limitation (second line). (k)–(o) CSI with true ROI limitation (third line). (p)–(t) CSI with initial ROI limitation (fourth line). (u)–(y) CSI with optimized ROI limitation (proposed method) (fifth line).

IV. Conclusion

We presented a microwave NDT observation model incorporating RPM radar imagery and the CSI-based reconstruction for to characterize embedded objects in concrete material. The general NDT model does not support omnidirectional data observation and the inverse problem for dielectric profile reconstruction becomes severely ill-posed. To resolve the above difficulty, this study proposed the ROI limitation scheme to enhance the accuracy of dielectric profile reconstruction by reducing the number of unknowns, the prior estimation of the ROI was achieved by an effective radar approach known as the RPM method. In addition, it introduced the ROI optimizing scheme using the CSI cost function, to provide a more accurate ROI. That is, one direction from the RPM to the CSI improves the reconstruction performance of complex permittivity, whereas the other direction from the CSI to RPM contributes to the ROI optimization, resulting in a bi-directional optimizing scheme between radar and tomography. Since the ROI is determined by the RPM, our proposed method does not need any prior knowledge of the target shape, even in the ROI update scheme. The 2-D FDTD-based numerical simulations for the NDT observation model demonstrated that the ROI limitation scheme considerably enhances the reconstruction accuracy, compared with that without ROI limitation, especially in challenging scenarios. In addition, the estimation accuracy of the ROI was enhanced: the size and location of buried objects were accurately determined, which would not be possible through a single use of the RPM method or other radar imaging methods. Note that the original or proposed CSI method is used in an arbitrary shape, size, or location of objects because the domain integration equation in (2), which is the basis of CSI can be satisfied regardless of the object's position, shape, or dielectric profile. However, in a realistic situation, a rustic component is expected to adhere to the surface of metallic pipes and such complicate scenarios should be assessed in our future study.

REFERENCES

[1] S. Agarwal and D. Singh, "An adaptive statistical approach for non-destructive underline crack detection of ceramic tiles using millimeter wave imaging radar for industrial application," *IEEE Sensors J.*, vol. 15, no. 12, pp. 7036–7044, Dec. 2015.

[2] J. Park and C. Nguyen, "An ultrawide-band microwave radar sensor for nondestructive evaluation of pavement subsurface," *IEEE Sensors J.*, vol. 5, no. 5, pp. 942–949, Oct. 2005.

[3] M. Fallahpour, J. T. Case, M. Ghasr, and R. Zoughi, "Piecewise and Wiener filter-based SAR techniques for monostatic microwave imaging of layered structures," *IEEE Trans. Antennas Propag.*, vol. 62, no. 1, pp. 1–13, Jan. 2014.

[4] M. D. Buhari, G. Y. Tian, and R. Tiwari, "Microwave-based SAR technique for pipeline inspection using autofocus range-Doppler algorithm," *IEEE Sensors J.*, vol. 19, no. 5, pp. 1777–1787, Mar. 2019.

[5] F. Soldovieri, A. Brancaccio, G. Prisco, G. Leone, and R. Pierri, "A Kirchhoff-based shape reconstruction algorithm for the multi-monostatic configuration: The realistic case of buried pipes," *IEEE Trans. Geosci. Remote Sens.*, vol. 46, no. 10, pp. 3031–3038, Oct. 2008.

[6] X. Zhuge, A. G. Yarovoy, T. Savelyev, and L. Ligthart, "Modified Kirchhoff migration for UWB MIMO array-based radar imaging," *IEEE Trans. Geosci. Remote Sens.*, vol. 48, no. 6, pp. 2692–2703, Jun. 2010.

[7] S. Kidera, T. Sakamoto, and T. Sato, "Accurate UWB radar 3-D imaging algorithm for complex boundary without range point connections," *IEEE Trans. Geosci. Remote Sens.*, vol. 48, no. 4, pp. 1993–2004, Apr. 2010.

[8] K. Akune, S. Kidera, and T. Kirimoto, "Accurate and nonparametric imaging algorithm for targets buried in dielectric medium for UWB radars," *IEICE Trans. Electron.*, vol. 95, no. 8, pp. 1389–1398, Aug. 2012.

[9] T. Manaka, S. Kidera, and T. Kirimoto, "Experimental study on embedded object imaging method with range point suppression of creeping wave for UWB radars," *IEICE Trans. Electron.*, vol. 99, no. 1, pp. 138–142, 2016.

[10] S. Takahashi and S. Kidera, "Acceleration of range points migration-based microwave imaging for nondestructive testing," *IEEE Antennas Wireless Propag. Lett.*, vol. 17, no. 4, pp. 702–705, Apr. 2018.

[11] R. Zoughi, *Microwave Nondestructive Testing and Evaluation*. Dordrecht, The Netherlands: Kluwer Academic, 2000.

[12] G. Govind, N. K. Tiwari, K. K. Agrawal, and M. J. Akhtar, "Microwave subsurface imaging of composite structures using complementary split ring resonators," *IEEE Sensors J.*, vol. 18, no. 18, pp. 7442–7449, Sep. 2018.

[13] J.-L. Hu, Z. Wu, H. McCann, L. E. Davis, and C.-G. Xie, "Quasi-three-dimensional method of moments for analyzing electromagnetic wave scattering in microwave tomography systems," *IEEE Sensors J.*, vol. 5, no. 2, pp. 216–223, Apr. 2005.

[14] W. C. Chew and Y. M. Wang, "Reconstruction of two-dimensional permittivity distribution using the distorted Born iterative method," *IEEE Trans. Med. Imag.*, vol. 9, no. 2, pp. 218–225, Jun. 1990.

[15] D. W. Winters, B. D. Van Veen, and S. C. Hagness, "A sparsity regularization approach to the electromagnetic inverse scattering problem," *IEEE Trans. Antennas Propag.*, vol. 58, no. 1, pp. 145–154, Jan. 2010.

[16] P. M. van den Berg and R. E. Kleinman, "A contrast source inversion method," *Inverse Problems*, vol. 13, no. 6, pp. 1607–1620, Jul. 1997.

[17] P. M. van den Berg, A. L. V. Broekhoven, and A. Abubakar, "Extended contrast source inversion," *Inverse Problems*, vol. 15, no. 5, pp. 1325–1344, 1999.

[18] A. Zakaria and J. LoVetri, "Application of multiplicative regularization to the finite-element contrast source inversion method," *IEEE Trans. Antennas Propag.*, vol. 59, no. 9, pp. 3495–3498, Sep. 2011.

[19] S. Sun, B. J. Kooij, T. Jin, and A. G. Yarovoy, "Cross-correlated contrast source inversion," *IEEE Trans. Antennas Propag.*, vol. 65, no. 5, pp. 2592–2603, May 2017.

[20] E. A. Attardo, G. Vecchi, and L. Crocco, "Contrast source extended Born inversion in noncanonical scenarios via FEM modeling," *IEEE Trans. Antennas Propag.*, vol. 62, no. 9, pp. 4674–4685, Sep. 2014.

[21] A. Zakaria and J. LoVetri, "The finite-element method contrast source inversion algorithm for 2D transverse electric vectorial problems," *IEEE Trans. Antennas Propag.*, vol. 60, no. 10, pp. 4757–4765, Oct. 2012.

[22] A. Abubakar, P. M. van den Berg, and J. J. Mallorqui, "Imaging of biomedical data using a multiplicative regularized contrast source inversion method," *IEEE Trans. Microw. Theory Techn.*, vol. 50, no. 7, pp. 1761–1771, Jul. 2002.

[23] H. Sato and S. Kidera, "ROI limited unknowns reduction-based contrast source inversion for microwave breast imaging," *IEEE Antennas Wireless Propag. Lett.*, vol. 19, no. 12, pp. 2285–2289, Dec. 2020.

[24] C. Kaye, I. Jeffrey, and J. LoVetri, "Improvement of multi-frequency microwave breast imaging through frequency cycling and tissue-dependent mapping," *IEEE Trans. Antennas Propag.*, vol. 67, no. 11, pp. 7087–7096, Nov. 2019.

[25] S. Sun, B. J. Kooij, and A. G. Yarovoy, "Linearized 3-D electromagnetic contrast source inversion and its applications to half-space configurations," *IEEE Trans. Geosci. Remote Sens.*, vol. 55, no. 6, pp. 3475–3487, Jun. 2017.

[26] R. Marklein, J. Miao, M. Rahman, and K. J. Langenberg, "Inverse scattering and imaging in NDT: Recent applications and advances," in *Proc. Eur. Conf. Non-Destructive Test.*, Sep. 2006, pp. 1–8.

[27] L.-P. Song, Q. H. Liu, F. Li, and Z. Q. Zhang, "Reconstruction of three-dimensional objects in layered media: Numerical experiments," *IEEE Trans. Antennas Propag.*, vol. 53, no. 4, pp. 1556–1561, Apr. 2005.

[28] M. A. Ali and M. Moghaddam, "3D nonlinear super-resolution microwave inversion technique using time-domain data," *IEEE Trans. Antennas Propag.*, vol. 58, no. 7, pp. 2327–2336, Jul. 2010.

[29] V. Schenone, A. Fedeli, C. Estatico, M. Pastorino, and A. Randazzo, "Experimental assessment of a novel hybrid scheme for quantitative GPR imaging," *IEEE Geosci. Remote Sens. Lett.*, vol. 19, pp. 1–5, 2022.

[30] M. Salucci et al., "2-D TM GPR imaging through a multiscaling multifrequency approach in L^p spaces," *IEEE Trans. Geosci. Remote Sens.*, vol. 59, no. 12, pp. 10011–10021, Dec. 2021.

[31] L.-P. Song, C. Yu, and Q. H. Liu, "Through-wall imaging (TWI) by radar: 2-D tomographic results and analyses," *IEEE Trans. Geosci. Remote Sens.*, vol. 43, no. 12, pp. 2793–2798, Dec. 2005.

[32] S. Sun, B. J. Kooij, T. Jin, and A. Yarovoy, "Through-wall imaging by TE and TM hybrid polarization inversion based on FDFD and frequency hopping scheme," in *Proc. IET Int. Radar Conf.*, 2015, pp. 1–8.

[33] A. Desmal and H. Bagci, "A preconditioned inexact Newton method for nonlinear sparse electromagnetic imaging," *IEEE Geosci. Remote Sens. Lett.*, vol. 12, no. 3, pp. 532–536, Mar. 2015.

[34] U. Taşkın and Ö. Özdemir, "Sparsity regularized nonlinear inversion for microwave imaging," *IEEE Geosci. Remote Sens. Lett.*, vol. 14, no. 12, pp. 2220–2224, Dec. 2017.

[35] L. Li, L. G. Wang, F. L. Teixeira, C. Liu, A. Nehorai, and T. J. Cui, "DeepNIS: Deep neural network for nonlinear electromagnetic inverse scattering," *IEEE Trans. Antennas Propag.*, vol. 67, no. 3, pp. 1819–1825, Mar. 2019.

[36] K. Xu, L. Wu, X. Ye, and X. Chen, "Deep learning-based inversion methods for solving inverse scattering problems with phaseless data," *IEEE Trans. Antennas Propag.*, vol. 68, no. 11, pp. 7457–7470, Nov. 2020.

[37] S. Takahashi and S. Kidera, "Efficient inverse scattering algorithm by incorporating RPM method for microwave non-destructive imaging," in *Proc. 26th Eur. Signal Process. Conf. (EUSIPCO)*, Sep. 2018, pp. 1222–1226.

[38] S. Takahashi and S. Kidera, "Incorporation algorithm with RPM and DBIM in Bayesian framework for microwave non-destructive testing," in *Proc. URSI Asia–Pacific Radio Sci. Conf. (AP-RASC)*, Mar. 2019, pp. 1–4.

[39] M. Benedetti, M. Donelli, D. Lesselier, and A. Massa, "A two-step inverse scattering procedure for the qualitative imaging of homogeneous cracks in known host media—Preliminary results," *IEEE Antennas Wireless Propag. Lett.*, vol. 6, pp. 592–595, 2007.

[40] O. Dorn and D. Lesselier, "Level set methods for inverse scattering," *Inverse Problems*, vol. 22, no. 4, pp. R67–R131, Aug. 2006.

[41] M. Salucci, L. Poli, N. Anselmi, and A. Massa, "Multi-scale compressive processing for inverse scattering within the contrast source formulation," in *Proc. IEEE Int. Symp. Antennas Propag. USNC-URSI Radio Sci. Meeting*, Jul. 2019, pp. 1017–1018.

[42] A. P. Dempster, N. M. Laird, and D. B. Rubin, "Maximum likelihood from incomplete data via the EM algorithm," *J. Roy. Stat. Soc. B, Methodol.*, vol. 39, no. 1, pp. 1–38, Feb. 1977.

Shuto Takahashi (Member, IEEE) received the B.E. degree in electrical and electronic engineering and the M.E. degree in informatics and communication engineering from The University of Electro-Communications, Chofu, Tokyo, Japan, in 2017 and 2019, respectively.

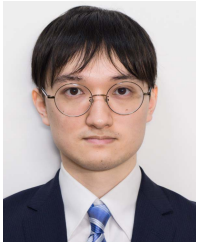

Katsuyoshi Suzuki received the B.E. degree in communication engineering and informatics from The University of Electro-Communications, Chofu, Tokyo, Japan, in 2021, where he is currently pursuing the M.E. degree with the Graduate School of Informatics and Engineering.

His research interests include inverse scattering and radar signal processing for microwave subsurface applications.

Takahiro Hanabusa received the B.E. degree in communication engineering and informatics and the M.E. degree in informatics and communication engineering from The University of Electro-Communications, Chofu, Tokyo, Japan, in 2019 and 2021, respectively.

Shouhei Kidera (Senior Member, IEEE) received the B.E. degree in electrical and electronic engineering and the M.I. and Ph.D. degrees in informatics from Kyoto University, Kyoto, Japan, in 2003, 2005, and 2007, respectively.

He has been with the Graduate School of Informatics and Engineering, The University of Electro-Communications, Chofu, Tokyo, Japan, since 2009, where he is currently an Associate Professor. His current research interests include advanced radar signal processing or electromagnetic inverse scattering issue for ultra wideband (UWB) 3-D sensor or biomedical applications. He has been stayed at the Cross-Disciplinary Electromagnetics Laboratory, University of Wisconsin–Madison, as a Visiting Researcher, in 2016. He has been a Principal Investigator of the PRESTO Program, Japan Science and Technology Agency (JST), from 2017 to 2021.

Dr. Kidera is a Senior Member of the Institute of Electronics, Information, and Communication Engineers of Japan (IEICE), and a member of the Institute of Electrical Engineering of Japan (IEEJ) and the Japan Society of Applied Physics (JSAP). He was a recipient of the 2012 Ando Incentive Prize for the Study of Electronics, the 2013 Young Scientist's Prize by the Japanese Minister of Education, Culture, Sports, Science and Technology (MEXT), and the 2014 Funai Achievement Award.